Rare Metal Materials and Engineering
Volume 55, Issue 1, January 2026
Available online at www.rmme.ac.cn

Science Press

Cite this article as: Xie Jilin, Li Shimeng, Wang Yaping, et al. Microstructure and Properties of Mg/Fe Dissimilar Metal Joints Fabricated by Magnetic Pulse Welding[J]. Rare Metal Materials and Engineering, 2026, 55(01): 67-77. DOI: https://doi.org/10.12442/j.issn.1002-185X.20240798.

ARTICLE

Microstructure and Properties of Mg/Fe Dissimilar Metal Joints Fabricated by Magnetic Pulse Welding

Xie Jilin[1], Li Shimeng[1], Wang Yaping[1], Liu Dongya[2], Liu Xiaofang[3], Chen Yuhua[1]

[1] Key Laboratory of Extreme Manufacturing Technology for High-End Equipment, Nanchang Hangkong University, Nanchang 330063, China; [2] Ma'anshan Iron & Steel Company Limited, Ma'anshan 243003, China; [3] State Key Laboratory of Advanced Brazing Filler Metals and Technology, Zhengzhou 450001, China

Abstract: Dissimilar AZ31B magnesium alloy and DC56D steel were welded via AA1060 aluminum alloy by magnetic pulse welding. The effects of primary and secondary welding processes on the welded interface were comparatively investigated. Macroscopic morphology, microstructure, and interfacial structure of the joints were analyzed using scanning electron microscope, energy dispersive spectrometer, and X-ray diffractometer (XRD). The results show that magnetic pulse welding of dissimilar Mg/Fe metals is achieved using an Al interlayer, which acts as a bridge for deformation and diffusion. Specifically, the AZ31B/AA1060 interface exhibits a typical wavy morphology, and a transition zone exists at the joint interface, which may result in an extremely complex microstructure. The microstructure of this transition zone differs from that of AZ31B magnesium and 1060 Al alloys, and it is identified as brittle intermetallic compounds (IMCs) Al_3Mg_2 and $Al_{12}Mg_{17}$. The transition zone is mainly distributed on the Al side, with the maximum thickness of Al-side transition layer reaching approximately 13.53 μm. Incomplete melting layers with varying thicknesses are observed at the primary weld interface, while micron-sized hole defects appear in the transition zone of the secondary weld interface. The AA1060/DC56D interface is mainly straight, with only a small number of discontinuous transition zones distributed intermittently along the interface. These transition zones are characterized by the presence of the brittle IMC $FeAl_3$, with a maximum thickness of about 4 μm.

Key words: magnetic pulse welding; mechanical properties; microstructure; fracture morphology; primary and secondary welding

1 Introduction

Steel is a structural material with high strength, excellent plasticity, and good weldability. As the most widely used material in motor vehicles, it accounts for 55% of the total vehicle weight[1]. Magnesium (Mg) is one of the lightest structural metal materials with a density of 1.74 g/cm^3; this low density endows it with unique advantages compared with other structural materials[2]. Mg alloys exhibit high specific strength, high specific stiffness, low density, high damping capacity, electromagnetic shielding properties, good dimensional stability, thermal and electrical conductivity, as well as excellent castability, machinability, and recyclability. Thus, they are known as the "21st Century Green Engineering Materials"[3]. Therefore, joining Mg alloys to steel enhances the application value of Mg alloys and promotes the development of automotive lightweighting technology.

Dissimilar metal joints meet the material requirements of different working conditions while leveraging the performance advantages of each constituent metal. At ambient temperature, Mg exhibits a hexagonal close-packed (hcp) crystal structure and Fe has a body-centered cubic (bcc) structure. This structural difference results in an extremely low solid solubility (<0.00041%) between Mg and Fe. Additionally, Mg and Fe are likely to form intermetallic compounds (IMCs), and they differ significantly in physical properties, including melting temperature, thermal conductivity, coefficient of thermal expansion, and lattice structure[4]. These factors collectively pose a key challenge to the joining of Mg alloys and steel. Generally, two approaches are employed to achieve metallurgical bonding between Mg and Fe which have vastly different physical properties: direct

Received date: January 09, 2025
Corresponding author: Chen Yuhua, Ph. D., Professor, Key Laboratory of Extreme Manufacturing Technology for High-End Equipment, Nanchang Hangkong University, Nanchan 330063, P. R. China, E-mail: yuhuachen@nchu.edu.cn

interlayer addition[5] and alloying element incorporation into the base metals[6]. For instance, during friction stir welding of steel and Mg alloys, Fe-Al IMCs are formed to replace Fe-Mg IMCs which have inferior mechanical properties[7]. Depositing a Zn layer between AZ31 Mg alloy and steel can inhibit the formation of Fe-Mg IMCs[8]. The strength of the welded joints depends on the microstructure and thickness of the interlayer[9].

In addition, diffusion welding, fusion welding, resistance spot welding, and ultrasonic spot welding have also been applied to Mg/Fe joining, and these methods all follow the aforementioned approaches. For example, the successful diffusion joining of Mg and Fe was achieved by adding Cu[10–11] and Ni interlayers[12]. Song[13], Li[14], and Zhao[15] et al reduced the formation of IMCs in Mg/Fe laser welding via elemental modulation and the addition of Ni foils. Similarly, in experiments on Mg/Fe resistance spot welding and ultrasonic spot welding, Zn foils and Al-Si coatings were added[16–18]. These cases prove that interlayer addition is beneficial for enhancing the interfacial mechanical properties of Mg/Fe joints. However, partial solid-state Mg/Fe welds, especially those involving the interlayer field, are still unexplored.

In recent years, scholars have increasingly studied the application of high-speed impact welding for dissimilar alloy joining. Vaporative foil actuator welding (VFAW) is a solid-state impact joining process that achieves bonding between two plates by rapidly evaporating a foil: the resulting expanding gases propel the flyer plate toward the substrate at high velocity[19]. Du et al[20] successfully joined NiTi and Al-Mg alloys by the VFAW technique. The results indicated a correlation between interface morphology and welding parameters, and the joint performance increased firstly and then decreased. Magnetic pulse welding (MPW)[21] is another solid-state welding technique, which operates based on the principles of using electromagnetic force to drive high-speed collision between two materials, thereby generating metallurgical bonding. This technique is characterized by high efficiency, environment friendliness, simple operation, and easy automation. It is unlikely to form a heat-affected zone due to its ultra-fast processing speed, and fewer IMCs are formed in the joint[22]. Thus, it is very suitable for joining dissimilar metals such as Al/Mg[23–25]. Likewise, Wang et al[26] explored the formation principle of the Al/Cu interface, Li et al[27] used numerical simulation to revealed the formation mechanism of the interfacial wave, and Sapanathan et al[28] studied the nucleation and growth processes of pores. In addition, MPW is also widely used in Al/Fe welding[29]. Revelant research includes amorphization and recrystallization[30], fatigue fracture properties, the correlation between interface morphology and discharge energy, and the effect of Zn coatings on phase transitions during MPW of Al/Fe[31–33].

In this research, a three-layer composite structure of AZ31B Mg alloy/AA1060 aluminum alloy/DC56D steel was prepared via the MPW technique. Al was selected as the interlayer due to its good compatibility and reactivity with both Mg and Fe. The welding configuration was set as follows: AZ31B Mg alloy served as the fly plate, AA1060 served as the interlayer, and DC56D steel served as the substrate plate. The mechanical properties of welded joints, along with the fracture morphology, welding interface morphology, and interfacial microstructure were analyzed.

2 Experiment

2.1 Experimental equipment

MPW equipment used in this study was an electromagnetic pulse welding system designated as XtraPulse 75/25, manufactured by Chongqing Pulsa Technology Co., Ltd. This system has a maximum output voltage of 25 kV and a maximum discharge energy of 75 kJ, and it consists of three core components: a control system, an energy storage system, and a worktable. The control system serves as the nerve center of the entire MPW equipment, which is responsible for controlling the welding power source parameters and the energy output mode. The energy storage system incorporates inductive-capacitive circuits and some impedance actuators. When the capacitor discharges, a high-intensity current passes through the coil, creating a primary magnetic field. This field induces a powerful secondary current in the flyer plate. However, the direction of this secondary current is opposite to that of the coil current, resulting in a strong repulsive Lorentz force between the coil and the flyer plate. This force causes the flyer plate to collide with the substrate plate at an ultra-fast speed. The coils used in this study adopted an E-shaped configuration.

2.2 Materials and methods

MPW was used to join Mg alloy and steel with Al as the interlayer. AZ31B Mg alloy and DC56D steel served as the flyer plate and the substrate with dimensions of 40 mm×80 mm×1 mm and 40 mm×80 mm×0.7 mm, respectively. The interlayer was pure Al with dimensions of 40 mm×20 mm×0.2 mm, and the driver plate was also pure Al with dimensions of 40 mm×80 mm×1 mm. The chemical composition of these materials is detailed in Table 1. The surfaces of base materials

Table 1 Chemical composition of base metals (wt%)

Base metal	Element						
AZ31B	Mg	Mn	Si	Fe	Ni	Al	Zn
	Bal.	0.2	0.08	0.003	0.001	3.0	1.0
DC56D	Fe	C	S	Mn	P	Nb	Si
	Bal.	0.002	0.005	0.38	0.002	0.02	0.008
AA1060	Al	Cu	Si	Mg	Zn	Ti	Fe
	Bal.	0.05	0.25	0.04	0.06	0.03	0.35

were wiped with alcohol to ensure cleanliness before welding. MPW process was performed using the lap joint configuration, as depicted in Fig. 1a. A high-temperature-resistant plastic spacer was applied between the flyer plate and the substrate to ensure a certain initial gap during welding. During the welding process, when the coil is energized by a pulse current, it generates an alternating magnetic field, which induces a current in the flyer plate. This induced current interacts electromagnetically with the coil's magnetic field, generating a Lorentz force that drives the flyer plate to collide with the substrate at high speed, thereby forming a weld. The principle of MPW is shown in Fig. 1b. Two welding methods were used in this experiment: primary welding and secondary welding. Primary welding involves directly applying the Al interlayer on the Mg alloy flyer plate; the flyer plate then collides with the substrate and the interlayer to form a joint. Secondary welding, by contrast, begins with a 1 mm-thick Al plate as the driver plate, onto which an insulation layer is applied to prevent contact between the driver plate and the interlayer. Subsequently, the driver plate is connected to the Al interlayer and DC56D steel (substrate), after which the Mg alloy (as a flyer plate) is welded to this assembly. Specific schematic diagrams of these two welding methods are shown in Fig.1c and 1d.

The welding parameters in this study were set as follows: discharge energies of 26, 28, 30, and 32 kJ, and a fixed welding gap of 1.5 mm. Welded samples were obtained by both primary and secondary welding methods, resulting in a total of eight weld combinations; all these combinations were subjected to mechanical property testing. Based on the mechanical properties of the welded samples, two sets of parameters with the optimal overall performance were selected from the primary welding samples and the secondary welding samples for subsequent microstructural characterization and analysis.

To study the microstructure of the bonded interface, samples perpendicular to the circumferential weld seam were cut using wire electrical discharge machining. After cold mounting, the samples were subjected to rough grinding, fine grinding, and polishing treatments, which were executed using sandpaper. A scanning electron microscope (SEM, Phenom-XL-SED) and an energy dispersive spectrometer (EDS, Oxford INCAx-act) were used to analyze the interface morphology and microstructure of the welded joints. For the mechanical performance evaluation, an Instron 5540 precision tensile machine was employed to conduct tensile-shear tests on the welded joints, with a crosshead speed of 1.5 mm/min.

3 Results and Discussion

3.1 Macroscopic morphology of welded joints

The macroscopic morphologies of the primary and secondary welding AZ31B/DC56D MPW samples are shown in Fig.2. The total length of the welded zone is about 120 mm, and the overlap area is about 20 mm×40 mm. The deformed region of the AZ31B Mg alloy flyer plate is located in the overlap area, and the zone with the most severe deformation in this region exhibits an elliptical shape. The welded seam is situated in the area of maximum deformation.

The width of the maximum deformation area (S) of AZ31B/DC56D MPW samples under different discharge energies and welding methods is presented in Table 2. It is noted that the welding method has no significant effect on the width S, while the discharge energy does impact the width S: S increases with increasing the discharge energy, though the increment is small. Yuan et al[34] showed that the width S is affected by the combined effects of discharge energy, initial gap, and coil width. When the initial gap is kept constant, the flyer plate receives more energy as the discharge energy increases, resulting in a larger deformation degree. However, due to the constraints of coil width and initial gap, the deformation does not increase infinitely with increasing the discharge energy; instead, it reaches a peak value.

3.2 Effect of discharge energy on tensile properties

This study investigated the effects of different discharge

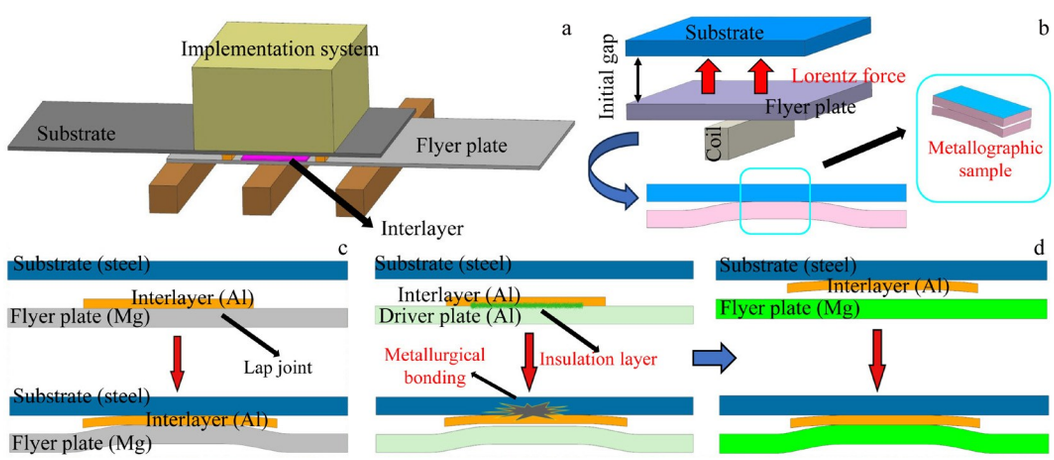

Fig.1 MPW process and principle schematic diagrams for AZ31B/AA1060/DC56D joining: (a) lap joint with interlayer; (b) MPW principle and sampling method; (c) primary welding (Fe, Al, and Mg plates were once welded); (d) secondary welding (Al and Fe bonding followed by Mg and Al bonding)

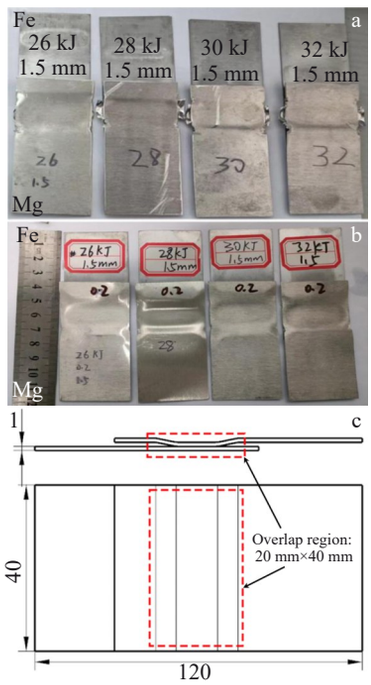

Fig.2 Macroscopic morphologies and size of MPW samples: (a) primary weld, (b) secondary weld, and (c) size specification of tensile sample of the lap joint

Table 2 Measurement values of joint size under different process parameters

Discharge energy/kJ	Initial gap/mm	Width/mm	
		Primary welding	Secondary welding
26	1.5	10.64	10.61
28		11.70	11.75
30		11.73	11.77
32		11.79	11.81

energies and welding techniques on the mechanical properties of Mg/Fe joints. The load-displacement curves of the joints fabricated via primary welding and secondary welding at varying discharge energies are illustrated in Fig. 3a and 3b, respectively. As depicted in Fig. 3, the mechanical properties of the joints prepared by both methods show a trend of increasing first and then decreasing with the increase in discharge energy. When the discharge energy is 28 kJ, the loads of welded joints reach their maximum values, resulting in interface failure. However, as shown in Fig. 3, the mechanical performance of the joints fabricated via the secondary welding process is superior to that of the primary welding joints. Further in-depth studies were conducted on the secondary welding joints.

As the thickness of Al interlayer is only 0.2 mm, the interlayer is basically detached from both Mg and Fe sides after tensile fracture. To better analyze the macroscopic fracture morphology, secondary welding samples with cleaner and more obvious fracture features were selected for observation. Tensile-shear test results and failure modes of the secondary welding joints are shown in Fig. 3c. Notably, the only failure mode observed at the joints is welded zone failure, which corresponds to interfacial failure on the Mg side. The actual photographs of the failed Mg alloy welded joints are also shown in Fig. 3c. The fracture morphology shows an elliptical weld, which is identified as a valid weld, with the width of the weld channel being about 1 mm. In MPW, a jet can only form on the surface of the welded metals when the collision speed and angle are within the optimal range; this jet is critical for achieving good metallurgical bonding between the metals. However, in the central region of the weld, although the collision velocity is sufficiently high, the collision angle is too small to induce jet formation on the metal surface. So, an annular welding seam is formed instead[35].

To elucidate the mechanisms responsible for weld quality variations, the microstructural evolution of the primary welding and secondary welding was analyzed using SEM under different process parameters: discharge energies of 28 and 32 kJ, and a fixed welding gap of 1.5 mm. Fig. 4 shows SEM cross-sectional micrographs of AZ31B/DC56D MPW joints with an Al interlayer. Fig.4a and 4b display the interface morphologies of primary welds under the discharge energies of 28 and 32 kJ, respectively. In Fig. 4a, the Mg/Al interface and the Al/Fe interface are straight, while the Al side of the Al/Fe interface contains an incomplete fusion zone, which consists of unfused Al and Fe agglomerates and a molten

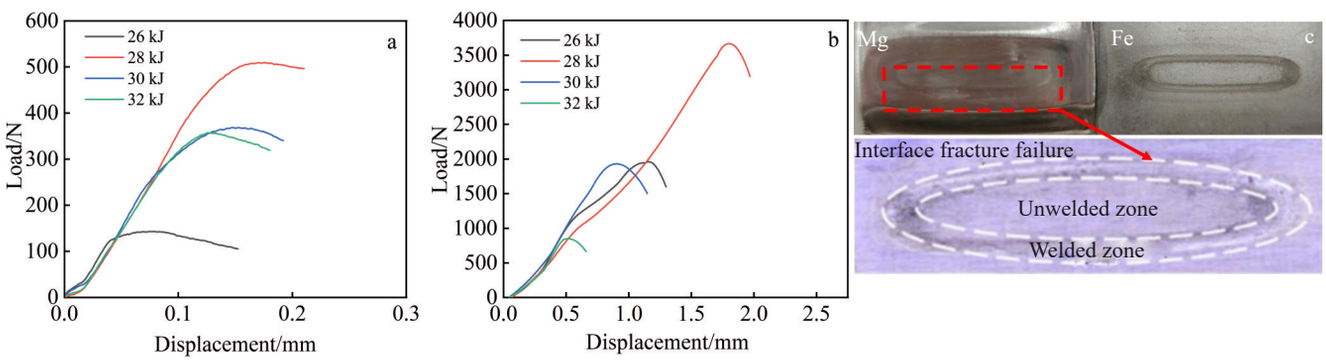

Fig.3 Load-displacement curves of Mg/Fe joints fabricated via primary welding (a) and secondary welding (b); fracture morphologies of Mg/Fe joints (c)

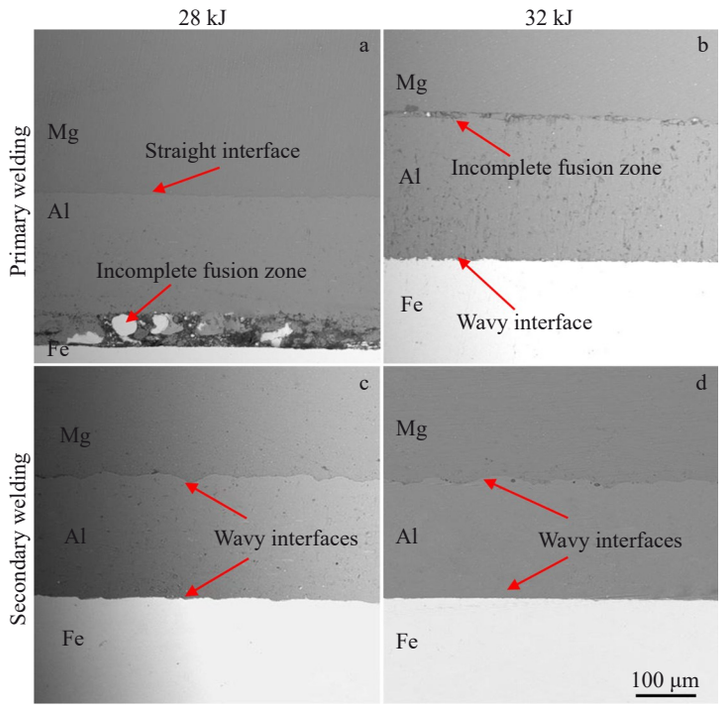

Fig.4 SEM images of Mg/Al/Fe bonding interface under different conditions

mixed structure. In Fig. 4b, bulk unfused structures are observed at the Mg/Al interface, and the Al/Fe interface exhibits wavy morphology (less distinct than the incomplete fusion features in Fig.4a). The metal jet spatters solidify at the interface, and the subsequent MPW process is insufficient to remelt these solidified spatters, resulting in unmelted metal particles at the interface. Similarly, incomplete fusion particles have been reported in Al/Ti MPW joints, where they were found to reduce the mechanical properties of the joints[36]. Fig.4c and 4d display the interface morphologies of secondary welds. It is apparent that there are two weld zones on both sides of the interlayer. The Mg alloy/Al interlayer and Al interlayer-steel interfaces exhibit wavy patterns. It is evident that there is still a straight interface at the Al/Fe boundary, and the wavy amplitude is minimal. Based on the above observations, the discharge energy in the primary welding is randomly distributed between the two interfaces, resulting in inferior interfacial bonding. As discharge energy increases, the interfacial waveform changes and the number of unfused structures decreases. In contrast, secondary welding does not suffer from this energy imbalance during the single welding process. Faes et al[37] found plastically deformed steel fragments at the interface of MPW-bonded Cu/steel tubes, which was attributed to insufficient elemental diffusion and mixing. This findings is also confirmed by Patra et al[38].

To observe the evolution of the welded interface in detail, the welded interface was observed using high-magnification SEM and EDS. Fig. 5 shows the typical morphologies of primary welds. By comparing the interfaces at different discharge energies, two key trends are identified: (1) with the increase in discharge energy, the welded interface changes from a straight to a wavy morphology; (2) the thickness of the transition layer increases. For the sample treated at 28 kJ, the Al/Fe interface exhibits varying degrees of wrinkling, which was not found in the sample treated at 32 kJ. This wrinkling phenomenon is attributed to insufficient discharge energy, which leads to plastic deformation at the interface. In addition, the morphology and the thickness of the transition layer at the Mg/Al and Fe/Al interfaces are inconsistent, which is caused by differences in the physical properties of Mg, Al, and Fe. EDS line scanning results of the corresponding areas in Fig. 5 further confirm that the increasing discharge energy expands the range of elemental diffusion, which is more obvious at the Mg/Al interface. A clear elemental platform phase can be found in the EDS results along line III, which suggests the generation of new phases in this area. The analysis results of points 1–4 in Fig. 5 are presented in Table 3. It can be found that a greater number of IMCs are generated at the Mg/Al interface, which is the main reason why the mechanical properties of samples treated by primary welding at 32 kJ are inferior to those at 28 kJ.

Fig. 6 illustrates typical SEM images of the bonded interfaces in the secondary welds. Fig.6a–6d and 6e–6h show the microscopic morphologies of the Mg/Al and Al/Fe interfaces, respectively. These micrographs demonstrate significant differences in dimensional characteristics of the interfacial waves, which is due to the dynamic changes in impact angle and collision velocity during the MPW process[39–40]. In addition, the wave morphologies at the interfaces are non-sinusoidal, due to the hardness discrepancy between the two base materials (Mg alloy and steel). When the discharge energy is increased, the wavy structure at the Mg/Al interface undergoes a tangible transformation: it shifts from a regular wave pattern to an irregular one. The Mg/Al

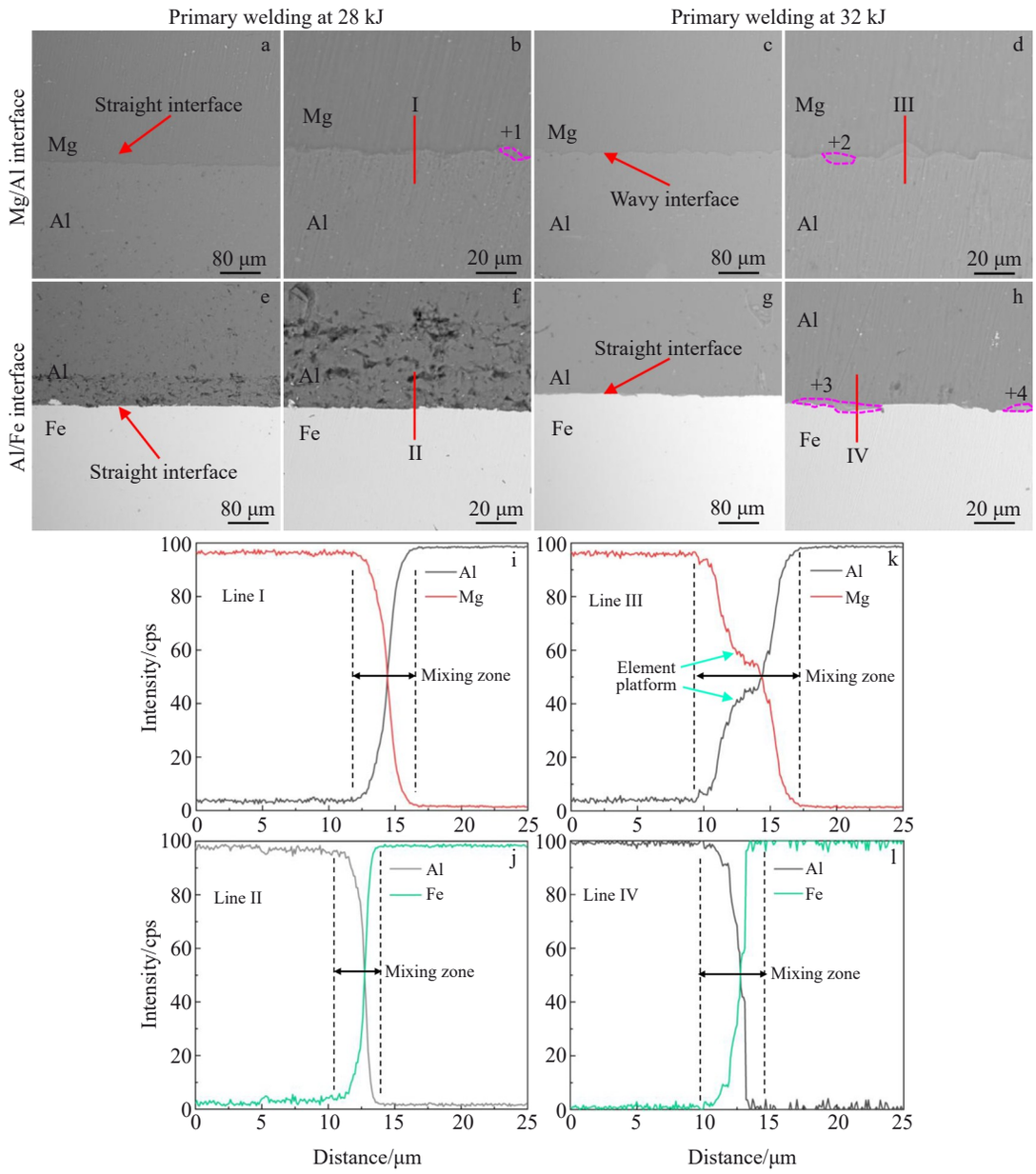

Fig.5 SEM images (a–h) and EDS line scanning results along lines I–IV (i–l) of Mg/Al/Fe bonding interfaces at different discharge energies

Table 3 EDS results for points marked in Fig.5 (at%)

Point	Mg	Al	Fe	Possible phase
1	55.06	44.94	-	Al_3Mg_2+$Al_{12}Mg_{17}$
2	60.57	39.43	-	$Al_{12}Mg_{17}$
3	-	90.26	9.74	Solid solution of Al
4	-	73.70	26.30	$FeAl_3$+Al

interface contains a transition zone, which is primarily distributed on the Al side. As discharge energy increases, the transition zone evolves from a discontinuous distribution to a continuous one in the wavy interface area, and its maximum thickness reaches 13.53 μm, as indicated by dotted areas in Fig.6b and 6d. The presence of hole defects is observed in the Mg/Al interfacial transition zone when the discharge energy is 32 kJ. These defects include micron-sized holes (indicated by blue arrows) and submicron-sized holes (indicated by white arrows) in Fig. 6c – 6d. The actual mechanism of such hole formation remains under investigation, but some scholars have suggested that interfacial voids are created by localized melting and subsequent solidification of the interfacial material[41–42]. Collectively, the presence of thicker transition zones and hole defects causes the reduced quality of their welded joints. The discharge energy has a minimal impact on the wave morphology of the Al/Fe interface, as shown in Fig. 6e – 6h. There is a transition zone at the Al/Fe interface, and it also exists on the Al side, as shown by the dotted areas in Fig. 6f and 6h. To form the transition zone, it is suggested that the high-speed impact during MPW causes intense plastic deformation of the interfacial material, resulting in heat accumulation at the weld interface and the formation of a localized high-temperature environment. Meanwhile, high

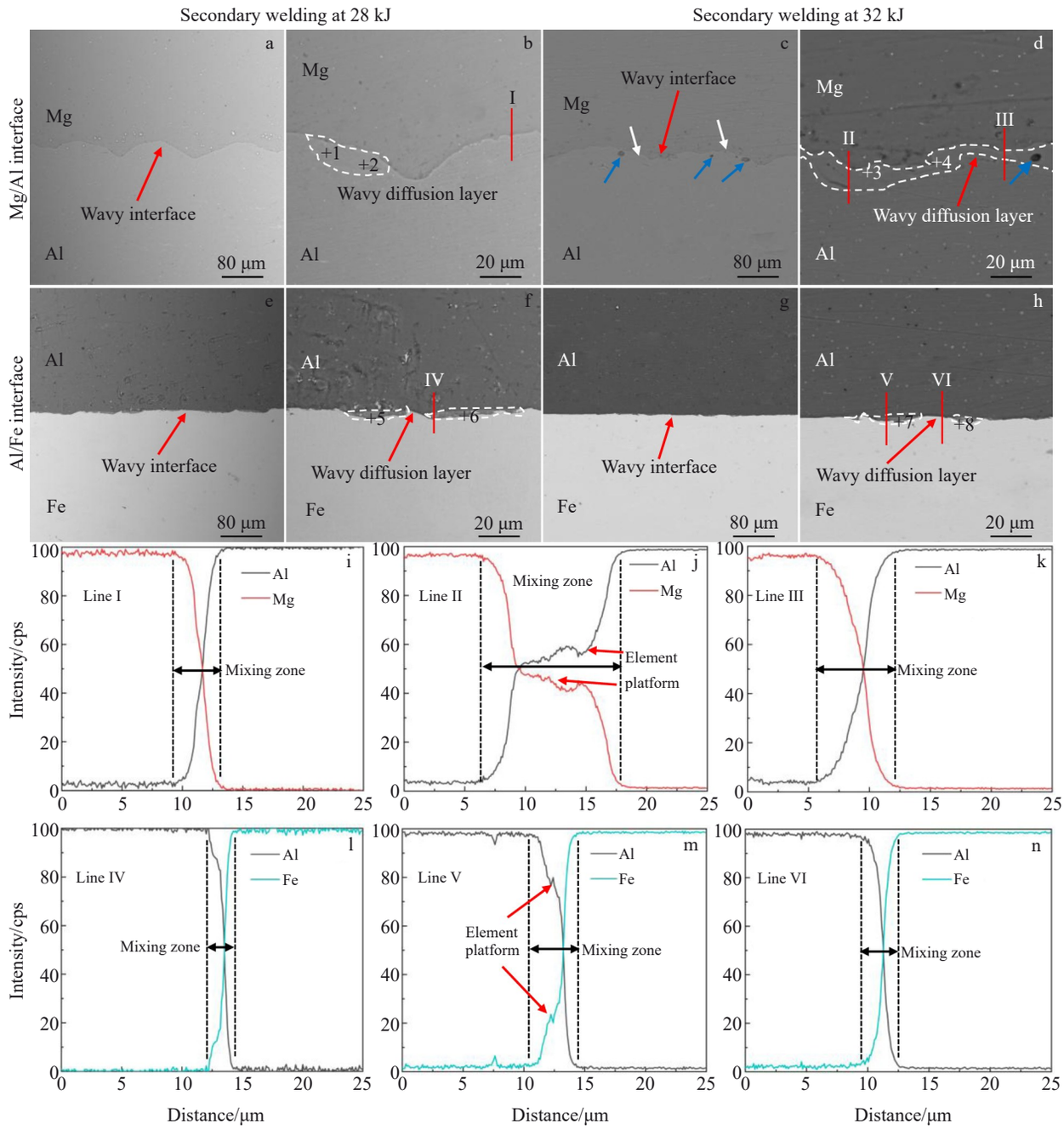

Fig.6 SEM images (a–h) and EDS line scanning results along lines I–VI (i–n) of Mg/Al/Fe bonding interfaces at different discharge energies

pressure, high temperature, and elemental concentration gradients promote the atomic migration and diffusion in localized areas of the weld interface, and migrating and diffusing atoms in high-temperature areas lead to formation of transition zones[43]. To establish a transition zone in the wavy interface, as depicted in Fig. 6f and 6h, it is suggested that an energy transfer process occurs during the collision, which is hindered by periodically distributed wave crests. This causes kinetic energy to be converted into thermal energy at the weld interface, leading to localized heat accumulation, atom migration, and diffusion, and subsequently forming a transition zone in the trough regions[44].

To study the in-depth microstructure of the secondary welding interfaces, EDS line scanning and point scanning analyses were performed on both the Mg/Al and Al/Fe weld interfaces. As shown in EDS results along lines I–VI, a certain degree of elemental diffusion occurs at both interfaces. Due to rapid high-pressure and high-temperature conditions in the MPW process, which result in a plastic deformation effect, matrix metal atoms near the interface undergo infiltration and convection, ultimately leading to mutual diffusion[45]. EDS line scanning results of Mg/Al interface (lines I–III) indicate that, in the reaction zone containing the transition zone, the maximum diffusion width of Mg and Al elements is approximately 13.53 μm. In comparison, the maximum width of the reaction layer in the non-transition zone is

approximately 3 μm. The melting and mixing of base metals on both sides of the interface can produce extremely complex microstructures in the transition zone. The Mg content in the transition zone is slightly lower than the Al content, and there is an approximate plateau between the two elements, as shown in EDS results of line II. It is difficult to explain this change from the point of view of elemental diffusion theory alone. By comparing it with the line scanning results of the non-transition region (lines I – III), it can be surmised that this transition region produces Mg compounds. Based on the atomic composition ratios, the Mg-Al alloy phase diagram[46], and EDS point scanning results in Table 4, it can be deduced that the transition region of the Mg/Al bonding interface consists of $Al_{12}Mg_{17}$ IMCs at a discharge energy of 28 kJ, and the transition region contains mixed IMCs of Al_3Mg_2 and $Al_{12}Mg_{17}$ at a discharge energy of 32 kJ. XRD analysis was performed on the Mg-side tensile fracture of the secondary welding sample at a difcharge energy of 28 kJ (Fig. 7). It can be seen that the Mg has the strongest diffraction peak, while no Al is detected, indicating that interfacial failure occurs on the Mg side of the interface. Additionally, the $Al_{12}Mg_{17}$ phase is identified in the fractured regions, which conforms to the $Al_{12}Mg_{17}$ formation at the Mg/Al interface. Elemental interdiffusion between Al and Fe is also observed at the Al/Fe bonding interface, as shown in EDS results of lines IV – VI. Elemental line scanning results also show that the diffusion widths of elements Al and Fe are about 4 μm in the transition zone and about 1.5 μm in the non-transition zone, with a plateau-like concentration distribution in the line scanning of the transition zone. Point scanning results (Table 4) reveal that the atomic percentages of Al and Fe are about 87% and 13%, respectively. Based on the Al-Fe alloy phase diagram[47], it can be deduced that the transition zone contains $FeAl_3$ IMCs and an Al-based solid solution. Compared with the Al/Fe interface, the Mg/Al interface has a thicker and more continuous transition zone, resulting in failures on the Mg side. Furthermore, the transition zone evolves from a discontinuous distribution to a continuous distribution, with increasing the discharge energy, and hole defects are generated in the transition zone. These factors collectively lead to the degradation of joint performance at higher energies[48].

Table 4 EDS results for points marked in Fig.6 (at%)

Point	Mg	Al	Fe	Possible phase
1	51.28	48.72	-	$Al_{12}Mg_{17}$
2	59.99	40.01	-	$Al_{12}Mg_{17}$
3	40.77	59.23	-	Al_3Mg_2+$Al_{12}Mg_{17}$
4	45.54	54.06	-	Al_3Mg_2+$Al_{12}Mg_{17}$
5	-	87.30	12.70	$FeAl_3$+Al
6	-	90.85	9.15	Solid solution of Al
7	-	87.72	12.28	$FeAl_3$+Al
8	-	90.26	9.74	Solid solution of Al

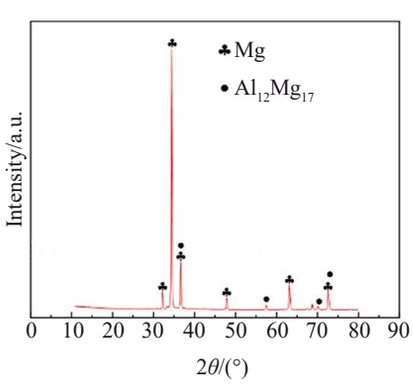

Fig.7 XRD pattern of Mg-side fracture section

The comparison of Fig. 5 and Fig. 6 shows that the interfacial diffusion layer of the secondary welds is thicker than that of the primary welding, which suggests that secondary welding has a more complete elemental distribution at the interface than the primary welds. This is confirmed in the EDS line scanning plots. The primary welding interfaces are generally straight, while the secondary welding interfaces show a wavy morphology, and the higher the discharge energy, the more the shear waves. A cross-comparison of Table 3 and Table 4 reveal that, although secondary welds have thicker diffusion layers and transition zones than primary welds, they also generate a greater quantity of IMCs and pore defects. In the comparison of the Mg/Al and Fe/Al interfaces of primary and secondary welds, the evolution of the Mg/Al interface is more drastic than that of the Fe/Al interface under both discharge energies; for primary welding, the discharge energy tends to be allocated to the Mg/Al interface, whereas in secondary welding process, the evolution of this interface stems from the inherent differences in the physical properties of the metal materials themselves[49–50].

3.3 Fracture morphology and failure analysis

To comprehend the bonding mechanism and fracture failure mechanism of the welded joints, the fracture morphologies of samples under various discharge energies were analyzed. The fracture morphologies and corresponding EDS elemental analysis results of primary welds are shown in Fig. 8. The interfaces of both fracture types exhibit a relatively flat morphology. At the Fe/Al interface, microcracks are generated after fracture; combined with Fig. 4a – 4b, it can be seen that numerous incompletely melted particles in the Fe/Al transition zone lead to microcracks during fracture. In contrast, Mg/Al interfacial transition layer contains fewer incompletely melted particles, and thus no microcracks are detected. EDS elemental distribution analysis of the fracture surfaces reveals no significant mutual diffusion of elements across the interface, which indicates that the primary welding interfaces exhibit insufficient bonding. In summary, the fracture of primary welding interfaces is attributed to the incompletely melted particles and limited elemental diffusion distance. The former causes stress concentration during the tensile-shear test, and the latter results in weak metallurgical bonding at the interface.

Fig. 9 shows the interfacial characteristics and EDS point scanning analysis results of secondary weldning fractures

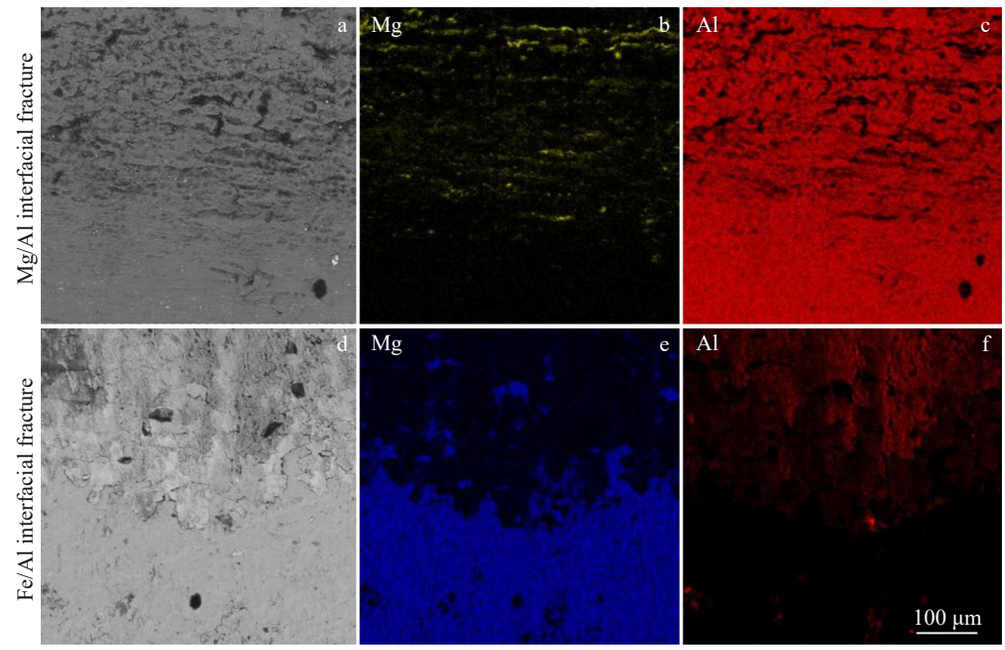

Fig.8 Typical fracture morphologies (a, d) and corresponding EDS elemental distributions (b–c, e–f) of primary welding at discharge energy of 28 kJ

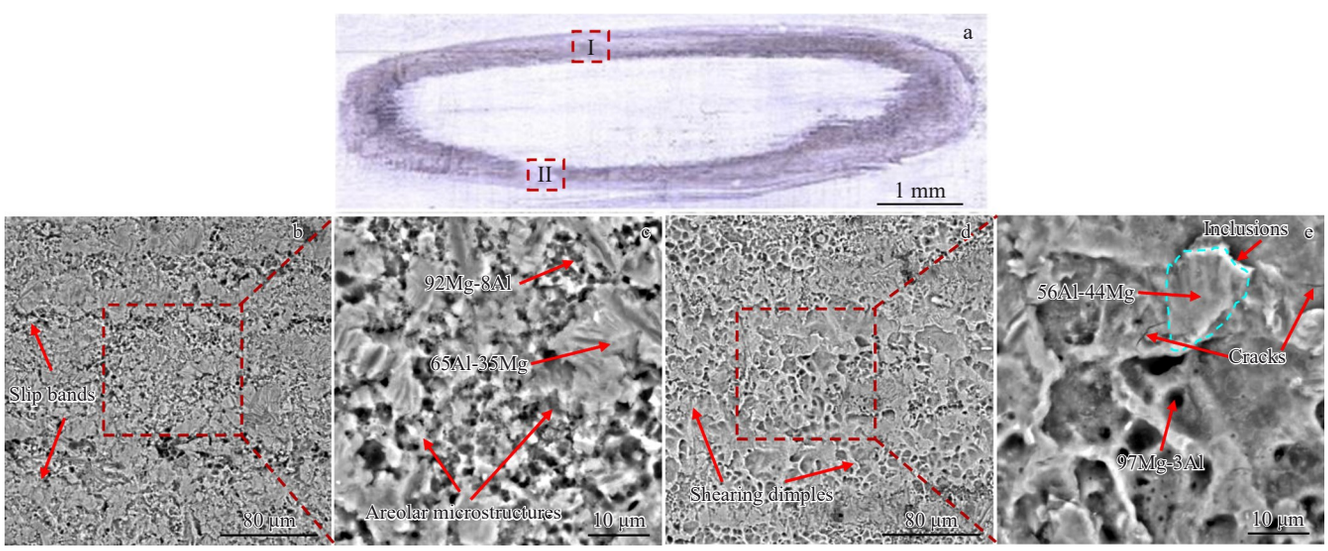

Fig.9 Tensile lap-shear fracture morphology at Mg side for MPW-bonded Mg-Fe dissimilar joint (a); magnified images of zone I (b) and zone II (d) in Fig.9a; magnified images of dotted areas in Fig.9b (c) and Fig.9d (e)

under a discharge energy of 28 kJ. Since fractures are concentrated on the Mg/Al side, different locations within the annular weld were selected for analysis. A macroscopic view of the annular bonding region where Mg-side interface failure occurs is illustrated in Fig. 9a. High-magnification views of zones I and II in the Mg-side weld (Fig. 9a) are shown in Fig. 9b and 9d, respectively. In zone I, the fracture is characterized by brittle fracture, and the section is dominated by a loose porous structure. EDS analysis of this zone shows the coexistence of elements Mg and Al. Based on previous analysis, the fracture occurs in the transition zone of the weld interface. Fractures in zone II are dominated by shear dimples which vary in size and are continuously distributed. In MPW, ultra-fast-velocity collision creates numerous cavities in the ligamentous fossa region, potentially leading to the instantaneous generation of highly non-equilibrium solidified eutectic structures[51]. According to the EDS analysis, the dimples are primarily composed of Mg, while some inclusions within the dimples contain both Mg and Al. As supported by the XRD results in Fig. 7, these inclusions may form a Mg-Al highly non-equilibrium solidified pseudo-eutectic structure. This shows that there is a coupling effect of shear stress and

bending moment due to this asymmetric structure in the tensile test process. The outer edge of the annular weld is prone to stress concentration, causing cracks to initiate first at this location. These cracks then propagate to the shear dimple area and ultimately spread to the entire inner-edge annular bonding area, leading to complete interfacial failure.

4 Conclusions

1) The interfacial transition zone and its morphology of primary and secondary welding AZ31B/DC56D MPW joints are mainly affected by discharge energy. For primary welding joints, the interfaces exhibit a flat morphology with an incomplete fusion layer. As the discharge energy increases, the thickness of this incompletely fusion layer gradually decreases, which is caused by the random distribution of energy during welding. For secondary welding joints, increasing discharge energy drives the interfacial morphology to transform from discontinuous waves to continuous shear waves, which also leads to the generation of micron-sized hole defects.

2) According to the bonding features of the interfacial transition zone, it can be concluded that the welded interfaces between Mg/Fe dissimilar materials and the Al interlayer are formed by the synergy of elemental mutual diffusion and mechanical bonding. In the MPW process, the Al interlayer acts as a bridge to achieve good weldability between Mg and Fe (two dissimilar materials) through its deformation and interfacial elemental diffusion.

3) Transition zones are observed at both the Mg/Al and Al/Fe welding interfaces. Specifically, the transition zone at the Mg/Al interface is composed of brittle IMCs Al_3Mg_2 and $Al_{12}Mg_{17}$, while the transition zone at the Al/Fe interface consists of brittle IMC $FeAl_3$.

Reference

1 Hovorun T P, Berladir K V, Pererva V I *et al. Journal of Engineering Sciences*[J], 2017, 4(2): 8

2 Jiang X Q, Chen S J. *Welding in the World*[J], 2018, 62(6): 1159

3 Ansari N, Alabtah F G, Albakri M I *et al. Journal of Magnesium and Alloys*[J], 2024, 12(4): 1283

4 Cheng J H, Hu X H, Sun X. *Computational Materials Science*[J], 2020, 185: 109988

5 Song G, Li T T, Yu J W *et al. Materials*[J], 2018, 11(12): 2515

6 Liu L, Xiao L, Feng J *et al. Scripta Materialia*[J], 2011, 65(11): 982

7 Kasai H, Morisada Y, Fujii H. *Materials Science and Engineering A*[J], 2015, 624: 250

8 Jana S, Hovanski Y, Grant G J. *Metallurgical and Materials Transactions A*[J], 2010, 41(12): 3173

9 Liu L M, Ren D X, Liu F. *Materials*[J], 2014, 7(5): 3735

10 Elthalabawy W M, Khan T I. *Materials Characterization*[J], 2010, 61(7): 703

11 Elthalabawy W M, Khan T I. *The International Journal of Advanced Manufacturing Technology*[J], 2011, 55(1–4): 235

12 Yuan X J, Sheng G M, Luo J *et al. Transactions of Nonferrous Metals Society of China*[J], 2013, 23(3): 599

13 Song G, Li T T, Chen L. *Materials Science and Engineering A*[J], 2018, 736: 306

14 Li T T, Song G, Yu P N *et al. Materials & Design*[J], 2019, 181: 107903

15 Zhao X Y, Wang D, Gao J M *et al. Journal of Materials Research and Technology*[J], 2022, 19: 4672

16 Liu L, Xiao L, Feng J C *et al. Metallurgical and Materials Transactions A*[J], 2010, 41(10): 2651

17 Zhang K P, Wu L J, Tan C W *et al. Journal of Materials Processing Technology*[J], 2019, 271: 23

18 Patel V K, Bhole S D, Chen D L. *Materials & Design*[J], 2013, 45: 236

19 Gong M Y, Lai Z P, Li C X *et al. Journal of Manufacturing Processes*[J], 2024, 131: 478.

20 Du F, Deng L, Wang X Y *et al. Journal of Materials Research and Technology*[J], 2022, 20: 3429

21 Prabu S S M, Aravindan S, Ghosh S *et al. Materials Today Communications*[J], 2023, 35: 105728

22 Kapil A, Sharma A. *Journal of Cleaner Production*[J], 2015, 100: 35

23 Chen Shujun, Yu Yang, Xia Yu *et al. Rare Metal Materials and Engineering*[J], 2013, 42(5): 998 (in Chinese)

24 Chen Shujun, Yu Yang, Xia Yu *et al. Rare Metal Materials and Engineering*[J], 2012, 41(2): 352 (in Chinese)

25 Zhu C C, Meng Y F, Liu Q X *et al. Precision Forming Engineering*[J], 2021, 13(4): 45

26 Wang P Q, Chen D L, Ran Y *et al. Materials Science and Engineering A*[J], 2020, 792: 139842

27 Li J S, Sapanathan T, Raoelison R N *et al. Journal of Materials Processing Technology*[J], 2021, 296: 117185

28 Sapanathan T, Raoelison R N, Buiron N *et al. Scripta Materialia*[J], 2017, 128: 10

29 Yang Y, Luo Z, Zhang Y X *et al. Journal of Manufacturing Processes*[J], 2024, 110: 376

30 Geng H H, Mao J Q, Zhang X *et al. Materials Letters*[J], 2019, 245: 151

31 Geng H H, Sun L Q, Li G Y *et al. International Journal of Fatigue*[J], 2019, 121: 146

32 Ghosh P, Patra S, Chatterjee S *et al. Journal of Materials Processing Technology*[J], 2018, 254: 25

33 Wang S L, Zhou B B, Zhang X *et al. Materials Science and Engineering A*[J], 2020, 788: 139425

34 Yuan Shuchun, Zhang Wentao, Chen Yuhua *et al. Electric Welding Machine*[J], 2022, 52(6): 118 (in Chinese)

35 Xie J L, Zhang W T, Chen Y H *et al. Materials Characterization*[J], 2022, 194: 112462

36 Zhang W T, Xie J L, Chen Y H *et al. Scripta Materialia*[J], 2022, 210: 114434

37 Faes K, Kwee I, De Waele W. *Metals*[J], 2019, 9(5): 514
38 Patra S, Arora K S, Shome M *et al. Journal of Materials Processing Technology*[J], 2017, 245: 278
39 Yan Y B, Zhang Z W, Shen W *et al. Materials Science and Engineering A*[J], 2010, 527(9): 2241
40 Xie J L, Peng C C, Xie W X *et al. Materials Reports*[J], 2023, 37(5): 175
41 Wu X, Shang J. *Journal of Manufacturing Science and Engineering*[J], 2014, 136(5): 51002
42 Oliveira I V, Cavaleiro A J, Taber G A *et al. Materials Design and Applications*[J], 2017, 65: 419
43 Geng H H, Xia Z H, Zhang X *et al. Materials Characterization*[J], 2018, 138: 229
44 Li Y, Yang D Z, Yang W Y *et al. Materials*[J], 2022, 15(16): 5519
45 Chen S J, Han Y, Gong W T *et al. The International Journal of Advanced Manufacturing Technology*[J], 2022, 120(11–12): 7115
46 Niu Shiyu. *Forming and Microstructure of FSLW Joints Based on Mg/Al Heterogeneous Materials with Added Zn*[D]. Shenyang: Shenyang Aerospace University, 2020 (in Chinese)
47 Atabaki M M, Nikodinovski M, Chenier P *et al. Journal for Manufacturing Science and Production*[J], 2014, 14(2): 59
48 Hu T H, Pan H, Zhu P *et al. Journal of Materials Research and Technology*[J], 2024, 30: 7076
49 Geng Huihui. *Study on Al-Fe Magnetic Pulse Welding and Its Joint Failure Mechanism*[D]. Changsha: Hunan University, 2021 (in Chinese)
50 Zhu Congcong. *Microstructure Evolution and Bonding Mechanism at the Interface of Al/Mg Heterogeneous Metal Magnetic Pulse Welding*[D]. Changsha: Hunan University, 2023 (in Chinese)
51 Wang Puquan. *Properties of Dissimilar Metal Magnetic Pulse Welded Joints and Interfacial Bonding Mechanism*[D]. Chengdu: Southwest University, 2023 (in Chinese)

镁/钢异种金属磁脉冲焊接接头组织和性能

谢吉林[1]，李诗梦[1]，王亚平[1]，刘东亚[2]，刘晓芳[3]，陈玉华[1]
(1. 南昌航空大学 高端装备极端制造江西省重点实验室，江西 南昌 330063)
(2. 马鞍山钢铁有限公司，安徽 马鞍山 243003)
(3. 高性能新型焊接材料全国重点实验室，河南 郑州 450001)

摘　要：采用磁脉冲焊接技术对AZ31B镁合金/DC56D钢异种不相容金属进行了焊接。对比研究了一次焊和二次焊对被焊界面的影响。通过扫描电子显微镜、能谱仪和X射线衍射仪等对焊接接头的宏观形貌、微观组织及界面结构进行了研究。结果表明，铝中间层通过变形和扩散作为桥梁，实现了镁/钢异种不相容金属的磁脉冲焊接。AZ31B/AA1060界面呈现出典型的波形界面，在接头界面中存在过渡区，过渡层中可能生成了非常复杂的微观组织结构，其组织明显不同于两侧的AZ31镁合金和1060铝组织，可能是Al_3Mg_2和$Al_{l2}Mg_{17}$的脆性金属间化合物。过渡区主要存在于铝侧，最厚处约为13.53 μm。在二次焊过渡区中发现微米级孔洞缺陷，一次焊界面出现不同厚度的不完全熔化层。AA1060/DC56D界面主要是平直界面，在接头界面中只有少量过渡区断续分布在界面上，过渡区存在$FeAl_3$脆性金属间化合物，最厚处约为4 μm。

关键词：磁脉冲焊接；力学性能；显微组织；断口形貌；一次焊和二次焊

作者简介：谢吉林，男，1990年生，博士，副教授，南昌航空大学高端装备极端制造江西省重点实验室，江西 南昌 330063，E-mail：xiejilin1990@126.com